Discovery of fibrotic intervertebral disc in mice

Jian He[1,2,8], Sha Huang[1,8], Pulin Yan[1], Yangyang Li[1], Huaijian Jin[1], Ou Hu[1], Jun Zhu[1], Peng Lin[1], Yingbo Wang[1], Liang Zhang[1], Yu Guo[3], Liting Wang[4], Jianhua Zhao[1], Yangli Xie[5], Lin Chen[5], Yu Lan[6], Bing Liu[7], Peng Liu[1,*], Yibo Gan[1,*]

[1]Department of Spine Surgery, Center of Orthopedics, State Key Laboratory of Trauma, Burn and Combined Injury, Daping Hospital, Army Medical University (Third Military Medical University), Chongqing 400042, China;

[2]Laboratory of Basic Medicine, The General Hospital of Western Theater Command, Chengdu 610031, China;

[3]Department of Radiology, Daping Hospital, Army Medical University (Third Military Medical University), Chongqing 400042, China;

[4]Biomedical Analysis Center, Army Medical University (Third Military Medical University), Chongqing 400038, China;

[5]Center of Bone Metabolism and Repair, State Key Laboratory of Trauma, Burns and Combined Injury, Trauma Center, Research Institute of Surgery, Laboratory for the Prevention and Rehabilitation of Military Training Related Injuries, Daping Hospital, Army Medical University (Third Military Medical University), Chongqing 400042, China;

[6]Key Laboratory for Regenerative Medicine of Ministry of Education, Institute of Hematology, School of Medicine, Jinan University, Guangzhou 510000, China;

[7]State Key Laboratory of Experimental Hematology, Haihe Laboratory of Cell Ecosystem, Institute of Hematology, Senior Department of Hematology, the Fifth Medical Center of Chinese PLA General Hospital, Beijing 100071, China;

[8]These authors contributed equally: Jian He and Sha Huang

*Correspondence: liupengd@163.com (P.Liu); yibogan@126.com (Y.Gan)

Keywords: intervertebral disc, disc degeneration, animal model, fibrosis, finite element model, mechanosensation

Abstract

Mechanical overload on the spine is a critical factor in the onset of intervertebral disc (IVD) degeneration. However, the lack of a precise and reliable animal model impedes a comprehensive understanding of the pathogenesis associated with IVD degeneration. In this study, we identified the high prevalence of spontaneous fibrotic alterations in IVDs predominantly located in the tail base, spanning from Co3/4 to Co5/6 levels, as early as 28 days in mice. These fibrotic IVDs manifested characteristics including extracellular matrix fibrosis and a decline in cell density. We leveraged a finite element model of computational biomechanics to generate fully predictive, three-dimensional simulations of flexion motion in the mouse tail. Our simulations revealed that the caudal discs in the mouse tail base underwent various mechanical overloads. Hence, we propose that the caudal IVDs in mice can serve as a novel mechanical model for investigating the mechanisms underlying the pathogenesis of IVD degeneration.

Introduction

Intervertebral disc degenerative diseases (DDD) are a leading cause of low back pain, significantly impacting the quality of life and emerging as a prominent public health concern. According to the latest statistics by WHO, low back pain and neck pain were the major contributors to disability-adjusted life years with 568 million people and 64 million years of life lived with disability globally[1], making it a great challenge associated with the world's population aging. Despite the high incidence of low back pain, the underlying mechanisms of DDD remain incompletely understood. As a result, treatment options are limited to providing symptomatic relief, rather than targeting the pathogenic factors of DDD. This has spurred the request for updating the understanding of the pathogenesis of DDD in order to protect human health.

The pathogenesis of DDD poses challenges in comprehensive understanding due to limited access to living human intervertebral discs (IVDs). To overcome this limitation, an alternative approach is to establish an accurate and bionic animal model, which holds promise in unraveling the pathogenesis and treatment of DDD[2]. Several animal models have been attempted to mimic the pathogenesis of DDD. For instance, animal models with genetic modification provide insights into the role of a specific gene or protein in DDD[3,4], but they fail to capture the complexity of multiple contributors. Models with acute IVD injury via needle puncture are commonly adopted due to their reproducible radiological and histological outcomes resembling DDD[5–9] , yet they fail to reflect the long-term mechanical overload associated with DDD[10]. Therefore, various approaches have been employed to develop mechanical DDD models, including surgically induced instability, compressive suture, tail-looping and external compression[11–14]. However, their complexity and reproducibility limit their widespread use in studying human DDD. Importantly, certain animal models, such as chondrodystrophic dog and sand rat, have been reported to develop spontaneous disc degeneration[15,16]. Nevertheless, the utilization of these animal models is limited by their high costs of breeding and housing, and the lengthy process of aging. Given these challenges, it is essential to develop animal models that are not only cost-effective and convenient but also offer a more precise depiction of human IVD pathology.

Previous studies have reported the presence of spontaneous age-related lumbar IVD degeneration in 14-month-old C57BL/6J (C57) mice and an increased dystrophic disc calcification in caudal discs with aging was also observed in LG/J mice[2,17]. Interestingly, early-onset disc degeneration were observed in SM/J mice owing to genetic contribution[18,19]. These studies suggest that mice can be used as a spontaneous animal model of DDD. Our

study uncovered the caudal discs in the tail base of regular C57BL/6 mouse strains subjected to mechanical overload during flexion motion, which mimics the mechanical conditions experienced by the lower lumbar discs in humans. Strikingly, we discovered a spontaneous IVD exhibiting fibrotic characteristics as early as 28 days postnatally in these IVDs located from Co3/4 to Co5/6 due to mechanical overload, with a prevalence of up to 82.9% in the Co4/5 disc. The fibrotic IVDs showed a distinct phenotype with extracellular matrix (ECM) fibrosis and a decline in cell density. These spontaneous fibrotic changes could be attributed to the exhaustion of notochord cells (NCs), heightened inflammation and increased mechanosensation, closely resembling the degenerative alterations in the lower lumbar disc of human. Taken together, these findings suggest that C57BL/6 mice can serve as a novel mechanical model and a valuable tool for investigating the mechanisms underlying the pathogenesis of DDD.

Results

Fibrotic IVDs are discovered in the tail base of one-month-old mice

We utilized a 7.0T T2-weightted MRI to explore the effect of mechanical overload across the six caudal disc levels of one-month-old mice (Fig. 1a). A significant decline in MRI index was found at the disc levels of the tail base (Co3/4, Co4/5 and Co5/6), indicating the loss of hydration of these discs (Fig.1a). Consistently, the mean T2 relaxation time in Co3/4, Co4/5, and Co5/6 was significantly lower than that of Co2/3, Co6/7 and Co7/8 (Fig.1b). These findings demonstrate the compromised hydration of the caudal discs in the tail base.

Furthermore, we isolated the caudal discs from Co2/3 to Co7/8 for histological evaluation. Strikingly, macroscopic differences of Co4/5 and Co5/6 discs compared to other discs were observed (Fig.1c). In contrast to the healthy IVDs fulfilled with extensive vacuolar network and proteoglycans, Co4/5 and Co5/6IVDs showed a loss of NP/AF demarcation, fewer NP cells, and the presence of clefts, resulting in significantly higher histological scores (Fig.1d)[20]. These results demonstrated that IVDs in the tail base were subjected to structural damage and dehydration. Consistent with the previous study[21], we found that T2 relaxation time and MRI index in this study exhibited a high correlation to the histological score of IVDs (Fig.1e). We also measured the disc height, another radiological index to assess the health state of IVDs across the levels. The results showed that the relative disc height of Co3/4, Co4/5 and Co5/6 discs was significantly lower than that of others (Fig.1f), suggesting the loss of disc height in the tail base.

These results collectively revealed a distinct type of IVDs bearing fibrotic characteristics in the caudal disc, which was designated as fibrotic IVD. Differing from the IVDs with classical morphology, which was designated as hydrated IVD, fibrotic IVDs are frequently found in disc levels with mechanical overload, with an incidence rate ranging from 45.7% to 82.9% in Co3/4, Co4/5 and Co5/6 levels. These IVDs were associated with low MRI index, short T2 relaxation time, reduction of disc height and fibrotic NP histomorphology (Fig.1g, h). Therefore, the Co3/4, Co4/5 and Co5/6 were defined as the fibrotic region owing to the high incidence of type fibrotic IVDs (Fig.1i). Our results provide the robustness of MRI and micro-CT, two non-invasive quantitative imaging techniques, in the determination of IVD types, in line with a previous comparative study[22]. The inherent difference between these two types of IVDs would be explored next.

Fibrotic IVDs exhibit phenotype of NP fibrosis and cell apoptosis

To further illustrate the difference in the ECM deposition between hydrated and fibrotic IVDs,

we evaluated the type of the mouse caudal IVDs using MRI prior to dissecting for Picro-Sirius Red staining. Polarized light imaging revealed an absence of collagen deposition in the NP of hydrated IVDs while fibrotic IVDs showed a higher deposition of collagenous fibers in the NP (Fig.2a), resulting in a significant elevation of fibrosis area in the NP of fibrotic IVD compared to that of hydrated IVD (Fig.2b). Quantification of polarized images showed a similar composition of collagenous fibers in the AF between hydrated and fibrotic IVDs (Fig.2c). Immunofluorescence further showed a decrease of ACAN (aggrecan) in the NP of fibrotic IVDs, with a domination of COL I (type I collagen) and COL II (type II collagen), when compared to that of hydrated IVDs (Fig.2d). Additionally, quantification revealed that turnovers of these ECM molecules were found mainly in the NP rather than the AF (Fig.2e). Considering that the superiority of COL II to ACAN determines the chondrocytes from NP cells[23,24], our data suggested that the ACAN-dominant gelatinous ECM in the NP of hydrated IVDs turns to a COL II-dominant firm ECM as hyaline or fibrous cartilage in the NP of fibrotic IVDs.

We then compared the cellularity between type H and F IVDs, and found a significant decline in cell composition in the NP of type F IVDs compared to type H IVDs (Fig.2f). To address this impaired cellularity, we performed TUNEL assay to assess the differences in cell apoptosis. Consistently, there were significantly more TUNEL-positive cells in the NP of type F IVDs than in type H IVDs, but no significant differences were observed in the AF (Fig.2g). This demonstrated that cell apoptosis in the NP contributes to the decline in cellularity in the fibrotic IVDs.

Taken together, we revealed that the fibrotic IVDs are featured with the increased ECM fibrosis and cell apoptosis in NP. Interestingly, these deteriorations were previously reported to be associated with aging[25], thus warranting further investigation.

Mechanical overload effects on the base of mouse caudal discs

Previous studies have suggested that the mouse disc could serve as a mechanical model for the human disc due to similar biomechanical properties[26]. To verify the hypothesis, we developed a FEM of the lumbo-sacro-coccygeal spine from L1 to the tail end of C57BL/6J mice (Fig.3a), and performed simulations of the realistic lateroflexion of a mouse tail (Fig.3b). We observed an increased concentration of force in the discs ranging from Co2/3 to Co5/6 of the tail base during the lateroflexion, and a concentrated moment in the Co3/4 to Co5/6 discs (Fig.3c). It has been reported that the long tails of mammals are exposed to high bending moments due to their weight, especially when carried without ground contact in a more or

less horizontal position[27]. This was demonstrated in our predictions of von Mises stresses on the caudal discs during lateroflexion, dorsiflexion, and plantarflexion (Fig.3d-f), which revealed a contrasting increase in the mechanical stress on the AF and EP of the Co3/4, Co4/5, and Co5/6 discs. And the highest von Mises stresses were observed on the Co4/5 disc during the motion in three directions (Fig.3h). We then compared the stress during the flexion of NP between two types of IVDs, and found that NP in fibrotic IVDs was exposed to higher mechanical stress than that in hydrated IVDs during tail flexion (Fig.3i). These results indicate that the discs in the mouse tail base were exposed to mechanical overload.

Taken together, our FEM revealed the mechanical overload on the caudal discs of the tail base in mice, Further investigation are required to determine the responses of these discs, which are susceptible to mechanical overload.

Discussion

The severe threat of DDD to human health prompted us to seek an innovative treatment for IVD regeneration. Nevertheless, the inadequate knowledge of the IVD physiology and pathology limited the advances in treatment strategies due to the scarcity of precise and reliable animal models simulating the pathogenesis of IVD deterioration. Previous studies have demonstrated that abnormal mechanical overload is a pathological hallmark of disc degeneration, which results in tissue trauma and/or adaptive changes of IVD[28,29]. Here, we discovered a high prevalence of spontaneous fibrotic IVDs in the mouse tail base at an early age, that were exposed to mechanical overload comparable to that of the lower lumbar disc in humans. Our study identified a valuable mechanical model that mimics the pathological progress of human IVD, providing a crucial tool for delving deeper into the underlying mechanisms responsible for DDD.

IVD functions as a shock absorber for the spine, providing load distribution, energy dissipation, and motion control in response to body weight and daily activities[30]. Prolonged and repetitive overload can lead to the accumulation of microtrauma in IVD, making them more susceptible to further injury and compromising their self-healing capability[28]. Thus, mechanical loading plays an extremely important role in the occurrence and development of IVD degeneration. Given that the gravity-induced mechanical overload to human IVD is significantly influenced by upright posture, previous attempts were made to utilize mammals including non-human primates and the bipedal mice, which were restricted by ethical and cost considerations[31,32]. To induce mechanical loading, several interventions have been adopted to reproduce disc degeneration, such as tail looping, external apparatus to apply axial

compression, asymmetrical compression and surgically induced instability [11,14,33–35]. Their utilization is constrained by concerns regarding the time required and the complexity involved. Importantly, muscle contraction and ligament tension also contribute to the overload to IVD, which is attributed to the greater challenge of stabilizing a horizontally aligned spine compared to a vertically balanced spine[36]. In this regard, our FEM simulation also revealed that multidirectional tail flexion initiated by ligament tension created mechanical overload on the IVD of mouse tail base (Fig.3). The phenomenon of mechanics-induced IVD fibrosis could be regarded as side effect of tail flexion beyond its primary role of maintaining body balance.

In contrast to the artificial mechanical interventions mentioned above, physiological tail flexion leads to spontaneous IVD fibrosis in early age. Mechanical overload accelerates senescence and bone diseases, such as osteoarthritis and skeletal muscle hypertrophy[37,38]. Our findings provide compelling evidence for premature aging IVD resulting from mechanical overload. Previous studies reported that it took at least 12 to 30 months to model spontaneous disc degeneration in sand rats[59], which is a time-consuming process in contrast to the spontaneous fibrotic IVD detected in mice in our study. Although mice are considered an ideal model for aging studies and widely used to characterize the aging of the spine, controversy has arisen regarding disc degeneration in mice, because the criteria of evaluation for aging-related disc degeneration was varied due to the discrepancies induced by MRI evaluation, histological scoring and so on[39–41]. Distinct from the findings that disc degeneration in mice ranges from 14 months to 24 months[2,42], our data combining MRI examination and histological scoring consistently suggested that IVD fibrosis occurs as early as one month in C57BL/6J mice, significantly advancing the onset time of disc deterioration. This could be attributed to the different mechanical conditions between cervical/ lumbar and caudal discs in mice[43]. Interestingly, spontaneous disc degeneration could be found in SM/J mice as early as two week and featured by a high abundance of hypertrophic collagen, which is associated with the vitamin D receptor (VDR) gene[19]. In contrast, we found that the discs in the tail base experience mechanical overload and inflammatory responses in C57 mice (Fig. 4). Despite the activation of these mechanosensation under the mechanical loading remains unknown, a recent study proposed that inflammatory signaling can sensitize Piezo1-induced mechanotransduction in articular chondrocytes, which could be a potential pathogenic feed-forward mechanism in osteoarthritis[44].

Examining the age-related degeneration of IVDs in mice in comparison to humans holds significant importance. However, the presence of degenerated discs in young individuals

suggests that non-age-related factors also play a substantial role in the pathogenesis of disease[45]. A previous study has identified two distinct patterns of lumbar disc degeneration in humans, including a subset with endplate changes in the upper lumbar disc and another with degenerative changes in the lower lumbar disc associated with age and BMI[46]. Intriguingly, we found a high prevalence of type F IVD in the mouse Co3-Co7 region, with the incidence rate reaching 82.9% in the Co4/5 disc, establishing it as a promising animal model for studying the pathogenesis of human disc degeneration.

Methods

Mice

The animal use followed the guidelines of the animal ethics committee of Third Military Medical University (AMUWEC20223385). C57BL/6J mice of one month old were purchased from the Experimental Animal Center of Third Military Medical University (China), SPF Biotechnology Co., Ltd (China), Vital River Laboratory Animal Technology Co., Ltd. (China) and Biocytogen Pharmaceuticals Co., Ltd, respectively. Mice were housed in the SPF-grade animal facility of Daping Hospital (Chongqing, China).

MRI

Forty-seven postnatal one-month-old mice were euthanized with an intraperitoneal injection of 0.8% pentobarbital sodium (80 mg.kg-1). Mid-sagittal images of all caudal IVDs were qualitatively analyzed using MRI to document the degenerative changes. More precisely, a 7.0 T micro-MRI machine (BioSpec 70/20 USR, BRUKER, Germany) was employed to acquire T2-weighed mid-sagittal images and qualitatively analyze T2 mapping of the discs, with a TurboRARE T2-weighted sequence (repetition time = 4000 ms; echo time = 30 ms; field of view =25×25 mm2; slice thickness = 0.4 mm) and T2 mapping sequence (repetition time = 3000 ms; echo times = 9, 18, 27, 36, 45, 54, 63, 72, 81, 90, 99, 108 ms; field of view = 25×25 mm2; slice thickness = 0.4 mm). ImageJ software (v1.54d, National Institutes of Health, USA) was used for the manual selection of the region of interest (ROI) for each IVD and quantitative analysis of the sagittal T2 image slices. T2 relaxation times were calculated using Image Display and processing ParaVision (v6.0.1, BRUKER, Germany). The MRI index (the average signal intensity) was used to quantify the hydration of observed IVDs, with normalization performed against the signal intensity of the upper vertebral bone. Three blinded observers evaluated the grade of degeneration on T2-weighted scans based on the Pfirrmann grading system[47].

Micro-computed tomography (micro-CT) analysis

To establish a finite element model for the motion of mouse tail, the specimens of vertebras from L1 to the tail end were harvested from the one-month-old mice and fixed in 4% PFA, stored in 70% EtOH, then scanned with a micro-CT system (Skyscan 1272, Bruker, German) with a resolution of 5 μm, 1300 ms exposure time, 65 kV source voltage and 153 μA source current along with a 0.25 mm aluminum filter. 3D reconstructions were generated by the NRecon Reconstruction software (Bruker, Germany). To quantitatively evaluate the disc

height, the specimens of coccygeal vertebras from Co2 to Co8 were harvested from the 1-month-old mice. Samples were scanned using the high-resolution micro-CT system (Skyscan 1276, Bruker, Germany) with a pixel size of 10 μm, 1014 ms exposure time, 50 kV source voltage, and 200 μA source current along with a 0.25 mm aluminum filter. The relative intervertebral disc height for each IVD was calculated along the mid-sagittal plane as previously described71[48].

Histological analysis

Dissected mouse spine specimens from Co2-8 were fixed in 4% paraformaldehyde for 48 hours, then decalcified in 15% EDTA for 20 days and embedded in paraffin. Serial mid-sagittal sections were cut into 3-μm-thickness slices for mouse spine specimens, and stained with hematoxylin/eosin, Safranin-O/ Fast Green (G1371, Solarbio, China) for histology assessment or Picro-Sirius Red (G1472, Solarbio, China) for visualization of collagen content. The staining was examined under a microscopy system (CX43 or VS200, Olympus, Japan) and analyzed using FCSnap (V1.1.21486, Olympus, Japan) or OlyVIA (V3.4.1, Olympus, Japan). Qualification of collagen composition was conducted according to a previous study[49]. To evaluate degeneration, mid-sagittal sections of 6 caudal discs per mouse were scored using a histological and reference system for the mouse IVD by four blinded observers[20].

Immunofluorescence staining

For immunostaining, deparaffinized sections were incubated with pepsin (ZLI9013, ZSGB-BIO, China) for 15 min and permeabilized with 1% Triton X-100 (Solorbio, T8200, China) for 15 min and blocked with 5% bovine serum albumin (Sigma, B2064, USA) for 30 min. Primary antibodies of anti-ACAN (1:50, 13880-1-AP, ThermoFisher, USA), anti-COL2α1 (1:50, ab185430, Abcam, UK), and anti-COL1α1 (1:100, ab34710, Abcam, UK) were used following a standard staining protocol. Note that mouse IVD specimens for immunostaining of anti-Col I and anti-Col II were embedded in OCT and cryosectioned at 16-μm-thickness. Subsequently, sections were incubated with Alexa FluorTM Plus 555 anti-mouse IgG secondary antibody (1:500, A32727, Invitrogen, USA) and Alexa Fluor® 555 anti-rabbit IgG secondary antibody (1:500, ab150062, Abcam, UK) for 1 h at room temperature. Finally, an antifade mounting medium with DAPI solution (Beyotime, P0131, China) was applied to visualize the cell nucleus. The immunostaining image was captured by the microscopy system (CX43, Olympus, Japan) and the confocal microscopy system (LSM900, ZEISS, Germany) and analyzed by imaging software (Zen 2.3, ZEISS, Germany).

TUNEL assay

TUNEL staining was performed using the In Situ Cell Death detection kit (Roche Diagnostic, USA). Briefly, sections were de-paraffinized and blocked with 3% H2O2 for 15 min, then incubated with pepsin for 15 min and treated with TUNEL assay reaction mixture at 37℃ for 1h. Antifade mounting medium with DAPI solution was applied to visualize the cell nucleus. The immunostaining image was captured by the microscopy confocal microscopy system. ImageJ was used for the quantification of TUNEL-positive cells.

Finite element model

FE model of a mouse spine from L1 to the tail end was constructed. Initially, the mouse tail was scanned using a micro-CT system as described above. The image files with DICOM format were converted into 3D model construction using image processing software (Mimics v17.0, Materialise, Belgium). The properties of tissues within the tail, such as muscle and tendon, were identified according to H&E staining and previous description[50], and then segmented and used to generate 3D surface models of each tissue type. These 3D surface models were imported into HyperMesh. A tetrahedral mesh was generated for each tissue type, with element size optimized to ensure model accuracy while minimizing computational cost. The mesh was checked for the quality using built-in metrics and any problematic areas were manually refined. Material properties were then assigned to each tissue type based on values reported in the literature (Supplementary Table 1). Finally, to simulate the steady relaxions, the lumbar spine was fully constrained to prevent rigid body motion, and a load applied as a displacement boundary condition, generating a 2 mm-displacement of the tendon at tail base. The force and moments for each IVD and von Mises stresses on the IVD components during the flexion were measured.

Statistical analysis

All statistical analyses were conducted in R (4.1.3). Statistical analyses are described in the relevant sections of the article. C57BL/6J mice from at least three commercial laboratories to avoid the housing environmental effect. The sample size was determined to ensure the sufficient standard deviations of the mean and biologically important difference between groups.

Data availability

The experimental data and their statistical analysis generated in this study are available from the corresponding authors upon reasonable request.

References

1. Cieza, A. *et al.* Global estimates of the need for rehabilitation based on the Global Burden of Disease study 2019: a systematic analysis for the Global Burden of Disease Study 2019. *The Lancet* **396**, 2006–2017 (2020).
2. Ohnishi, T., Sudo, H., Tsujimoto, T. & Iwasaki, N. Age-related spontaneous lumbar intervertebral disc degeneration in a mouse model: SPONTANEOUS MOUSE IVD DEGENERATION. *J. Orthop. Res.* (2017) doi:10.1002/jor.23634.
3. Gorth, D. J., Shapiro, I. M. & Risbud, M. V. A New Understanding of the Role of IL□1 in Age□Related Intervertebral Disc Degeneration in a Murine Model. *J. Bone Miner. Res.* **34**, 1531–1542 (2019).
4. Che, H. *et al.* p16 deficiency attenuates intervertebral disc degeneration by adjusting oxidative stress and nucleus pulposus cell cycle. *eLife* **9**, e52570 (2020).
5. Masuda, K. *et al.* A Novel Rabbit Model of Mild, Reproducible Disc Degeneration by an Anulus Needle Puncture: Correlation Between the Degree of Disc Injury and Radiological and Histological Appearances of Disc Degeneration: *Spine* **30**, 5–14 (2005).
6. Korecki, C. L., Costi, J. J. & Iatridis, J. C. Needle Puncture Injury Affects Intervertebral Disc Mechanics and Biology in an Organ Culture Model: *Spine* **33**, 235–241 (2008).
7. Zhang, H., La Marca, F., Hollister, S. J., Goldstein, S. A. & Lin, C.-Y. Developing consistently reproducible intervertebral disc degeneration at rat caudal spine by using needle puncture: Laboratory investigation. *J. Neurosurg. Spine* **10**, 522–530 (2009).
8. Martin, J. T. *et al.* Needle puncture injury causes acute and long-term mechanical deficiency in a mouse model of intervertebral disc degeneration: MECHANICAL DEFICIENCY FOLLOWING DISC INJURY. *J. Orthop. Res.* **31**, 1276–1282 (2013).
9. Zhang, Y. *et al.* Histological Features of the Degenerating Intervertebral Disc in a Goat Disc-Injury Model: *Spine* **36**, 1519–1527 (2011).
10. Sobajima, S. *et al.* A Slowly Progressive and Reproducible Animal Model of Intervertebral Disc Degeneration Characterized by MRI, X-Ray, and Histology: *Spine* **30**, 15–24 (2005).
11. Oichi, T. *et al.* A Mouse Intervertebral Disc Degeneration Model by Surgically Induced Instability. *Spine* **43**, E557–E564 (2018).
12. Liu, Z. *et al.* A novel in vivo mouse intervertebral disc degeneration model induced by compressive suture. *Exp. Cell Res.* **398**, 112359 (2021).
13. Nakamichi, R. *et al.* Mohawk promotes the maintenance and regeneration of the outer annulus fibrosus of intervertebral discs. *Nat. Commun.* **7**, 12503 (2016).
14. Lotz, J. C., Colliou, O. K., Chin, J. R., Duncan, N. A. & Liebenberg, E. 1998 Volvo Award Winner in Biomechanical Studies: Compression-Induced Degeneration of the Intervertebral Disc: An in Vivo Mouse Model and Finite-Element Study. *Spine* **23**, 2493–2506 (1998).
15. Melrose, J., Taylor, T. K. & Ghosh, P. Variation in intervertebral disc serine proteinase inhibitory proteins with ageing in a chondrodystrophoid (beagle) and a non-chondrodystrophoid (greyhound) canine breed. *Gerontology* **42**, 322–329 (1996).
16. Gruber, H. E., Johnson, T., Norton, H. J. & Hanley, E. N. The sand rat model for disc degeneration: radiologic characterization of age-related changes: cross-sectional and prospective analyses. *Spine* **27**, 230–234 (2002).
17. Novais, E. J. *et al.* Comparison of inbred mouse strains shows diverse phenotypic outcomes of intervertebral disc aging. *Aging Cell* **19**, (2020).
18. Choi, H. *et al.* A novel mouse model of intervertebral disc degeneration shows altered cell fate and matrix homeostasis. *Matrix Biol.* **70**, 102–122 (2018).
19. Zhang, Y. *et al.* Early onset of disc degeneration in SM/J mice is associated with changes in ion transport systems and fibrotic events. *Matrix Biol.* **70**, 123–139 (2018).
20. Tam, V. *et al.* Histological and reference system for the analysis of mouse intervertebral disc: HISTOLOGICAL GRADING OF MOUSE DISC. *J. Orthop. Res.* (2017) doi:10.1002/jor.23637.
21. Detiger, S. E. L. *et al.* MRI T2* mapping correlates with biochemistry and histology in intervertebral disc degeneration in a large animal model. *Eur. Spine J.* **24**, 1935–1943 (2015).
22. Piazza, M. *et al.* Quantitative MRI correlates with histological grade in a percutaneous needle injury mouse model of disc degeneration: MRI OF MOUSE DISC DEGENERATION. *J. Orthop. Res.* **36**, 2771–2779 (2018).
23. Gantenbein-Ritter, B., Benneker, L. M., Alini, M. & Grad, S. Differential response of human bone marrow stromal cells to either TGF-β1 or rhGDF-5. *Eur. Spine J.* **20**, 962–971 (2011).
24. Lady Davis Institute for Medical Research and Department of Surgery, SMBD-Jewish General Hospital, Montreal (QC) Canada, Mwale, F., Roughley, P. & Antoniou, J. Distinction between the extracellular matrix of the nucleus pulposus and hyaline cartilage: a requisite for tissue engineering of intervertebral disc. *Eur. Cells A¨nd Mater.* **8**, 58–64 (2004).
25. Olczyk, K. Age-related changes in proteoglycans of human intervertebral discs. *Z. Rheumatol.* **53**, 19–25

(1994).
26. Elliott, D. M. & Sarver, J. J. Young Investigator Award Winner: Validation of the Mouse and Rat Disc as Mechanical Models of the Human Lumbar Disc: *Spine* **29**, 713–722 (2004).
27. Preuschoft, H. & Klein, N. Torsion and Bending in the Neck and Tail of Sauropod Dinosaurs and the Function of Cervical Ribs: Insights from Functional Morphology and Biomechanics. *PLoS ONE* **8**, e78574 (2013).
28. Stokes, I. A. F. & Iatridis, J. C. Mechanical Conditions That Accelerate Intervertebral Disc Degeneration: Overload Versus Immobilization: *Spine* **29**, 2724–2732 (2004).
29. Desmoulin, G. T., Pradhan, V. & Milner, T. E. Mechanical Aspects of Intervertebral Disc Injury and Implications on Biomechanics. *Spine* **45**, E457–E464 (2020).
30. Setton, L. A. & Chen, J. Mechanobiology of the Intervertebral Disc and Relevance to Disc Degeneration. *J. Bone Jt. Surg.* **88**, 52–57 (2006).
31. Luk, K. D. K., Ruan, D. K., Chow, D. H. K. & Leong, J. C. Y. Intervertebral Disc Autografting in a Bipedal Animal Model: *Clin. Orthop.* **337**, 13–26 (1997).
32. Ao, X. *et al.* Development and Characterization of a Novel Bipedal Standing Mouse Model of Intervertebral Disc and Facet Joint Degeneration. *Clin. Orthop.* **477**, 1492–1504 (2019).
33. Sakai, D. *et al.* Migration of bone marrow–derived cells for endogenous repair in a new tail-looping disc degeneration model in the mouse: a pilot study. *Spine J.* **15**, 1356–1365 (2015).
34. Court, C. *et al.* The effect of static in vivo bending on the murine intervertebral disc. *Spine J.* **1**, 239–245 (2001).
35. Miyamoto, S., Yonenobu, K. & Oono, K. Experimental Cervical Spondylosis in the Mouse: *Spine* **16**, S495–S500 (1991).
36. Alini, M. *et al.* Are animal models useful for studying human disc disorders/degeneration? *Eur. Spine J.* **17**, 2–19 (2008).
37. Zhang, H. *et al.* Mechanical overloading promotes chondrocyte senescence and osteoarthritis development through downregulating FBXW7. *Ann. Rheum. Dis.* **81**, 676–686 (2022).
38. Roberts, M. D. *et al.* Mechanisms of mechanical overload-induced skeletal muscle hypertrophy: current understanding and future directions. *Physiol. Rev.* physrev.00039.2022 (2023) doi:10.1152/physrev.00039.2022.
39. Marfia, G. *et al.* Potential use of human adipose mesenchymal stromal cells for intervertebral disc regeneration: a preliminary study on biglycan-deficient murine model of chronic disc degeneration. *Arthritis Res. Ther.* **16**, 457 (2014).
40. Boyd, L. M. *et al.* Early-onset degeneration of the intervertebral disc and vertebral end plate in mice deficient in type IX collagen. *Arthritis Rheum.* **58**, 164–171 (2008).
41. Millecamps, M., Czerminski, J. T., Mathieu, A. P. & Stone, L. S. Behavioral signs of axial low back pain and motor impairment correlate with the severity of intervertebral disc degeneration in a mouse model. *Spine J.* **15**, 2524–2537 (2015).
42. Alvarez-Garcia, O., Matsuzaki, T., Olmer, M., Masuda, K. & Lotz, M. K. Age-related reduction in the expression of FOXO transcription factors and correlations with intervertebral disc degeneration: FOXO IN INTERVERTEBRAL DISC AGING. *J. Orthop. Res.* **35**, 2682–2691 (2017).
43. Sarver, J. J. & Elliott, D. M. Mechanical differences between lumbar and tail discs in the mouse. *J. Orthop. Res.* **23**, 150–155 (2005).
44. Wang, S. *et al.* Mechanical overloading induces GPX4-regulated chondrocyte ferroptosis in osteoarthritis via Piezo1 channel facilitated calcium influx. *J. Adv. Res.* **41**, 63–75 (2022).
45. Teraguchi, M. *et al.* Prevalence and distribution of intervertebral disc degeneration over the entire spine in a population-based cohort: the Wakayama Spine Study. *Osteoarthritis Cartilage* **22**, 104–110 (2014).
46. Li, Y. *et al.* Two subtypes of intervertebral disc degeneration distinguished by large-scale population-based study. *Spine J.* **16**, 1079–1089 (2016).
47. Pfirrmann, C. W. A., Metzdorf, A., Zanetti, M., Hodler, J. & Boos, N. Magnetic Resonance Classification of Lumbar Intervertebral Disc Degeneration: *Spine* **26**, 1873–1878 (2001).
48. Nishimura, K. & Mochida, J. Percutaneous Reinsertion of the Nucleus Pulposus: An Experimental Study. 20.
49. Johnston, S. N., Madhu, V., Shapiro, I. M. & Risbud, M. V. Conditional Deletion of HIF □2α in Mouse Nucleus Pulposus Reduces Fibrosis and Provides Mild and Transient Protection From Age□Dependent Structural Changes in Intervertebral Disc. *J. Bone Miner. Res.* **37**, 2512–2530 (2022).
50. Shinohara, H. The Musculature of the Mouse Tail is Characterized by Metameric Arrarmements of Bicipital Muscles. *Okajimas Folia Anat. Jpn.* **76**, 157–169 (1999).

Acknowledgements

This study was supported by grants from National Key Research and Development Program of China (2022YFA1103202), National Natural Science Foundation of China (32270887, 82272507 and 32200654), Postdoctoral Innovative Talent Support Program (BX20220397), the Open Project of State Key Laboratory of Trauma, Burns and Combined Injury (SFLKF202201 and SKLYQ201902), and Postgraduate Research Innovation Project of Chongqing Education Commission (CYS22751). The authors would like to thank Jimin Liu from Jiejun Technique Corporation (Chongqing, China) for his excellent contribution to the FEM construction. The authors are grateful to Wenxia Zheng from Olympus for the help with section staining and imaging.

Competing interests

The authors declare no competing interests.

Authors contribution

P. Liu, Y. Gan, and J. H. conceived and designed the study. B. L., Y. Lan, L. C., Y. X., and J. Z. provided research consultation. S. H., J.H., Y. Gan., P. Y., Y. Li, O. H., and J. Z. performed animal experiments and sampling. Y. Gan and J. H. conducted FEM analysis. Y. Guo, S. H., and Y. Gan performed radiological experiments. S. H. and P. Y. performed immunohistochemistry and immunofluorescence staining. L. W. and S. H. conducted confocal microscopy scanning. H. J., P. Lin, Y. W., and L. Z. performed statistical analysis. J. H., Y. Gan, and P. Liu designed the figures. Y. Gan, J. H., and P. Liu wrote the manuscript. All authors have read and approved the final manuscript.

Figure Legends

Fig.1 Imageology and histology identify the morphological characteristics of IVDs in mouse tail base.

a. Representative T2-weighted MRI (7T) of mouse tail spine across Co2 to Co8 (left). MRI index values of mouse tail IVDs (n = 47, right). *P* value was determined by Kruskal Wallis test.

b. Pseudo-color map of T2 relaxation time in mouse tail IVDs (left). Regions of interest (ROI) were manually drawn to indicate the IVD area. Black dots (right) show the average of T2 relaxation time values with the corresponding 95% confidence interval of each IVD from 47 mice (colored lines).

c. Representative Safranin O/Fast Green staining image of mouse tail spine across Co2 to Co8. The locations of IVDs are indicated. Cartilage (red), fiber, and bone (green). Scale bar, 1mm

d. Violin plots show histological scores of mouse tail IVDs (n = 10). Inner box plots indicate the 25th, median (middle line), 75th quartiles, and whiskers indicate the 5th and 95th percentiles, and single points indicate outliers. *P* value was determined by Kruskal Wallis test.

e. Scatter plot showing the correlations between histological scores and MRI T2 relaxation time (upper) and MRI index values (bottom). *P* value of Pearson correlation is calculated and linear regression is indicated by the line with 95% confidence interval.

f. Representative 3D micro-CT images of mouse tail vertebral body from Co2 to Co8 (left). The sagittal and horizontal micro-CT views are indicated. Violin plots show relative disc height of mouse tail IVDs (right, n = 10).

g. Representative hematoxylin-eosin (H&E) staining shows the morphology of two types of mouse tail IVD (n = 10 for each group). Scale bar, 100 μm

h. Stacked bar charts show the frequency of two types of IVD across Co2/3 to Co7/8. The type of IVDs is identified according to the Safranin O/Fast Green staining for each sample. The dashed line indicates the average proportion of fibrotic IVD in all samples (n = 35)

i. The diagram illustrates the distribution of fibrotic (orange shadow) and hydrated (light blue) IVDs in the mouse tail base.

Fig.2 Fibrotic IVDs show extracellular matrix fibrosis and a decline in cell density in NP.

a. Representative Picrosirius Red staining of hydrated and fibrotic IVDs in mouse tail under bright field (upper) and polarized light. Dash lines indicate the border between NP and AF. Scale bar, 100 μm

b. Violin plots show the proportions of fibrotic areas identified by Picrosirius Red staining in NP of hydrated and fibrotic IVDs (n = 10). *P* values of significances are determined by unpaired Student's t-test.

c. Stacked bar charts show the composition of AF collagen fiber in hydrated and fibrotic IVDs. The thickness of collagen fibers is indicated in green (Thin), yellow (Intermediate), and red (Thick). *P* values of significances between two types of IVD groups are determined by two-tailed Fisher's exact tests (n = 10).

d. Representative immunofluorescent staining of aggrecan (ACAN), Collagen type II (COL II) and Collagen type I (COL1) in hydrated and fibrotic IVDs.

e. Violin plots show the quantitative statistics of immunofluorescent staining density in whole IVD, NP, or AF, as indicated in **d.** (n = 15 in fibrotic IVD, n = 18 in hydrated IVD). *P* values of significances are determined by unpaired Student's t-test.

f. Stacked barplots show cell fractions of NP and AF in two types of IVD. *P* values of significances are determined by unpaired Student's t test.

g. Representative TUNEL staining of two types of IVD. Magnified view indicates the TUNEL positive cells in NP. Violin plots show the positive rates of NP and AF in two types of IVD (right). *P* values of significances are determined by unpaired Student's t test. Scale bar, 100 μm

Fig.3 FEM reveals the heightened mechanosensation in mouse tail base IVD.

a. Vertical view of FEM of mouse tail vertebra. Colored vertebral bodies indicate three anatomic parts including lumbar, sacral, and caudal discs. The muscle of tail base is indicated in flesh color and tendons across the caudal vertebra are indicated in gray. Magnified lateral view of Co2-Co8 is shown below.

b. Oblique view of FEM of mouse vertebra. The curved arrow indicates the lateroflexion. The force (red arrow) and moment (blue arrow) of each IVD are captured during the flexion.

c. Changes of force and moment of each IVD (colored lines) during the lateroflexion.

d-f. View of von Mises stress distributed in AF of mouse tail IVDs during lateroflexion (**d**), dorsiflexion (**e**) and plantarflexion (**f**). Magnified view showing the stress distribution of Co4/5 IVD.

g. Bar charts showing the stress of NP, AF and EP at the end of flexion.

h. View of von Mises stress distributed in NP between hydrated and fibrotic IVDs at the start and end of flexion. Smooth lines indicate linear regression 95% confidence interval of the average stress in NP of two type IVD (n = 3)

Figure 1

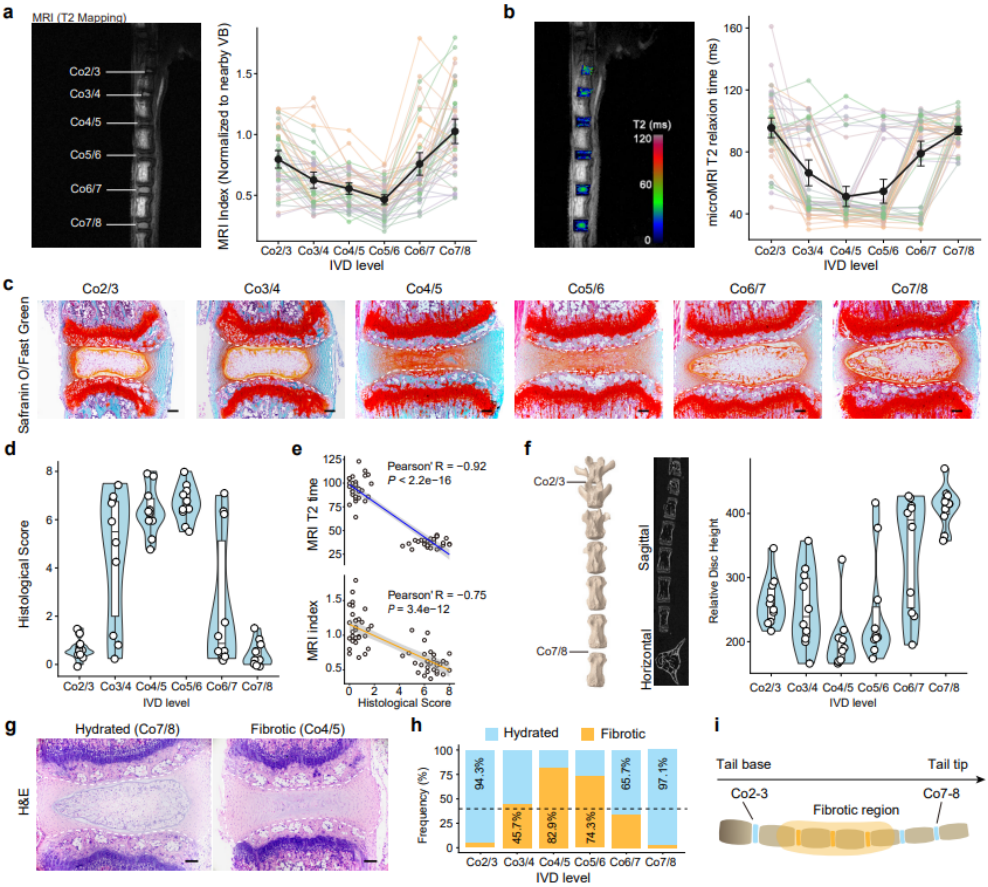
a
MRI (T2 Mapping)
Co2/3
Co3/4
Co4/5
Co5/6
Co6/7
Co7/8
MRI Index (Normalized to nearby VB)
IVD level
b
T2 (ms)
120
60
0
microMRI T2 relaxion time (ms)
IVD level
c
Safranin O/Fast Green
d
Histological Score
IVD level
e
MRI T2 time
Pearson' R = −0.92
P < 2.2e−16
MRI index
Pearson' R = −0.75
P = 3.4e−12
Histological Score
f
Sagittal
Horizontal
Relative Disc Height
IVD level
g
Hydrated (Co7/8)
Fibrotic (Co4/5)
H&E
h
Hydrated
Fibrotic
Frequency (%)
94.3%
45.7%
82.9%
74.3%
65.7%
97.1%
IVD level
i
Tail base
Tail tip
Co2-3
Co7-8
Fibrotic region

Figure 2

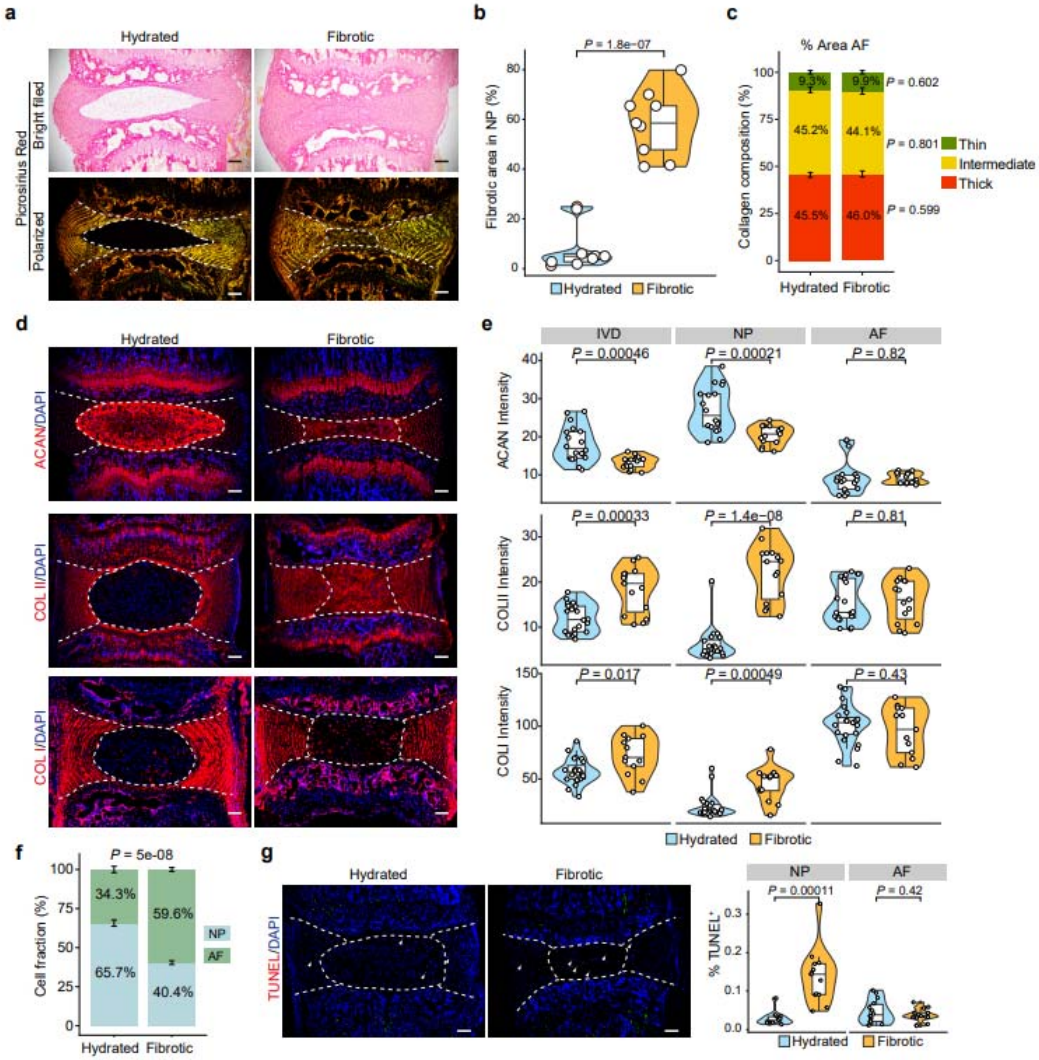
a
Hydrated
Fibrotic
Picrosirius Red
Bright filed
Polarized
b
P = 1.8e−07
Fibrotic area in NP (%)
Hydrated
Fibrotic
c
% Area AF
Collagen composition (%)
9.3%
9.9%
P = 0.602
45.2%
44.1%
P = 0.801
45.5%
46.0%
P = 0.599
Thin
Intermediate
Thick
Hydrated
Fibrotic
d
Hydrated
Fibrotic
ACAN/DAPI
COL II/DAPI
COL I/DAPI
e
IVD
NP
AF
ACAN Intensity
P = 0.00046
P = 0.00021
P = 0.82
COLII Intensity
P = 0.00033
P = 1.4e−08
P = 0.81
COLI Intensity
P = 0.017
P = 0.00049
P = 0.43
Hydrated
Fibrotic
f
P = 5e-08
Cell fraction (%)
34.3%
65.7%
59.6%
40.4%
NP
AF
Hydrated
Fibrotic
g
Hydrated
Fibrotic
TUNEL/DAPI
NP
AF
% TUNEL+
P = 0.00011
P = 0.42
Hydrated
Fibrotic

Figure 3

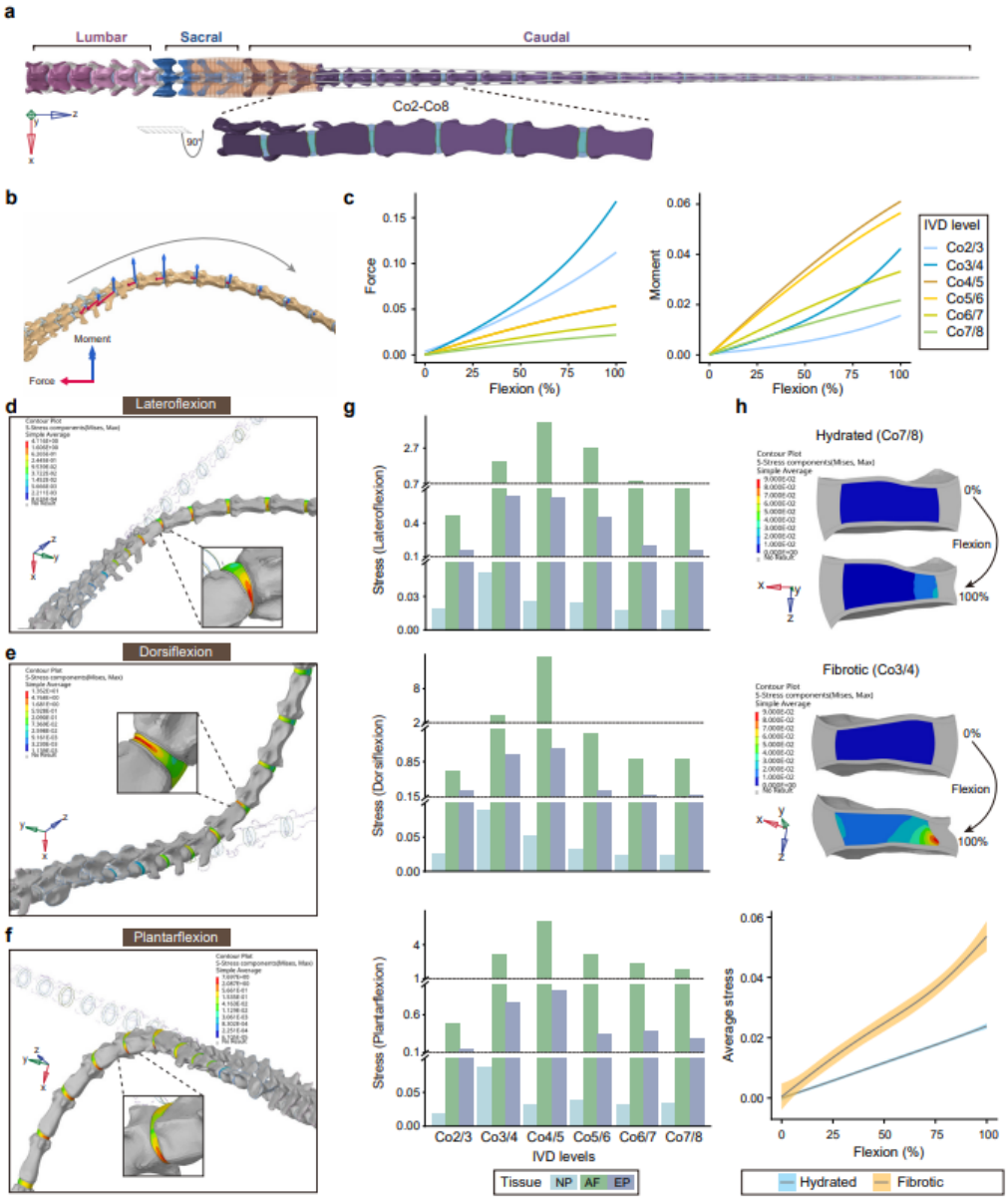
a
Lumbar
Sacral
Caudal
Co2-Co8
90°
b
Moment
Force
c
Force
Moment
Flexion (%)
IVD level
Co2/3
Co3/4
Co4/5
Co5/6
Co6/7
Co7/8
d
Lateroflexion
e
Dorsiflexion
f
Plantarflexion
g
Stress (Lateroflexion)
Stress (Dorsiflexion)
Stress (Plantarflexion)
IVD levels
Tissue
NP
AF
EP
h
Hydrated (Co7/8)
Fibrotic (Co3/4)
0%
Flexion
100%
Average stress
Hydrated
Fibrotic

554